A Perspective on LES and its Application to Liquid Rocket Combustion Systems

Joseph C. Oefelein
Sandia National Laboratories
Combustion Research Facility
Livermore, California 94551-0960

Abstract

This paper provides a perspective on Large Eddy Simulation (LES) and its application to liquid rocket injection, mixing and combustion processes. Simulating these processes involves a variety of challenges which include all of the classical closure problems inherent to the treatment of turbulence and combustion, and a unique set of problems imposed by the introduction of thermodynamic nonidealities and transport anomalies. Emphasis is placed on 1) the fundamental issues and limiting extremes, 2) the theoretical and numerical framework developed to handle these difficulties, and 3) a series of results which give insight into the intricate nature of the problem and current state of the art with respect to LES. The discussion is framed in the context of the three workshop test cases, with conclusions drawn accordingly.

Introduction

Simulating injection, mixing and combustion processes in cryogenic rocket engines poses a variety of challenges which include all of the classical closure problems inherent to the treatment of combustion, and a unique set of problems imposed by the introduction of thermodynamic nonidealities and transport anomalies. Flow conditions within the chamber are inherently turbulent, and combined demands associated with performance and heat transfer typically result in the specification of operating pressures and temperatures that produce local transcritical [1] and supercritical conditions.

From the classical point of view, reacting multiphase flows introduce the complicating factors of chemical kinetics, highly nonlinear source terms, and a variety of subgrid-scale (*sgs*) velocity and scalar mixing interactions. Flow field evolution is affected by compressibility effects (volumetric changes induced by changes in pressure) and variable inertia effects (volumetric changes induced by variable composition and/or heat addition). The resultant coupling yields an array of fluid dynamic, thermochemical, thermodynamic and transport processes which are dominated by widely disparate time and length scales.

The situation becomes more complex at elevated pressures due to the inherent decrease in turbulence scales and difficulties which arise as fluid states approach and/or exceed local critical conditions. Near the critical point, propellant mixture properties begin to exhibit liquid-like densities, gas-like diffusivities and pressure-dependent solubilities. Surface tension and heat of vaporization approach zero, and the isothermal compressibility and constant pressure specific heat increase significantly. These phenomena, coupled with extreme local property variations, have a significant impact on the evolutionary dynamics of a given system.

This paper presents a perspective on the Large Eddy Simulation (LES) technique and its application to the injection, mixing and combustion processes described above. After establishing the key phenomenological trends and flow characteristics, the implications, modeling options, and tradeoffs are outlined and the general requirements for LES are discussed and contrasted with the Reynolds-Averaged Navier-Stokes (RANS) approach. A series of case studies are then presented which highlight various aspects of the problem and the utility of LES as a fundamental tool. The discussion is framed in the context of the three workshop test cases, with conclusions drawn accordingly.

[1] A liquid propellant at subcritical temperature in a high-pressure supercritical environment.

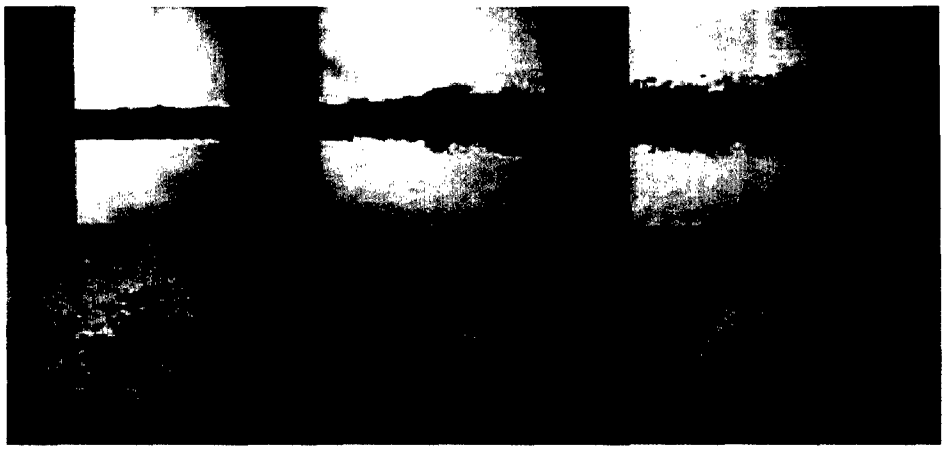

Figure 1: Reacting shear-coaxial liquid-oxygen–hydrogen injector operating at 1.5 *MPa* (15 atm). From Mayer and Tamura (1996). Used with permission.

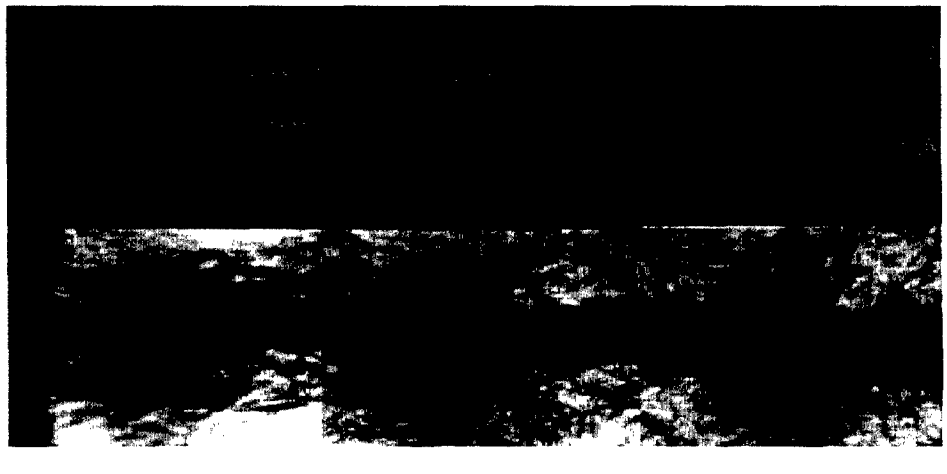

Figure 2: Reacting shear-coaxial liquid-oxygen–hydrogen injector operating at 4.5 *MPa* (44 atm). From Mayer and Tamura (1996). Used with permission.

Phenomenological Trends

Recent experiments have provided a much clearer understanding of the phenomenological conditions which exist as a function of chamber pressure. Depending on the injector type, fluid properties, and flow characteristics, two limiting extremes may exist. At subcritical chamber pressures, injected liquid jets undergo the classical cascade of processes associated with atomization. Dynamic forces and surface tension promote the formation of a heterogeneous spray which evolves continuously. Spray flames form as a consequence which are lifted away from the injector face in a manner consistent with the combustion mechanisms exhibited by local drop clusters. When chamber pressures approach or exceed the critical pressure of a particular propellant, however, injected liquid jets undergo a transcritical change of state as interfacial fluid temperatures rise above the critical temperature of the local mixture. For this situation, diminished intermolecular forces promote diffusion dominated processes prior to atomization and respective jets vaporize forming a continuous fluid in the presence of exceedingly large gradients. Well mixed diffusion flames evolve as a consequence which are anchored by small but intensive recirculation zones generated by the shearlayers imposed by adjacent propellant streams.

The flow visualization studies conducted by Mayer and Tamura (1996) illustrate these trends for the case of a liquid-oxygen–gaseous-hydrogen shear-coaxial injector element. The two extremes are shown in Figs. 1 and 2,

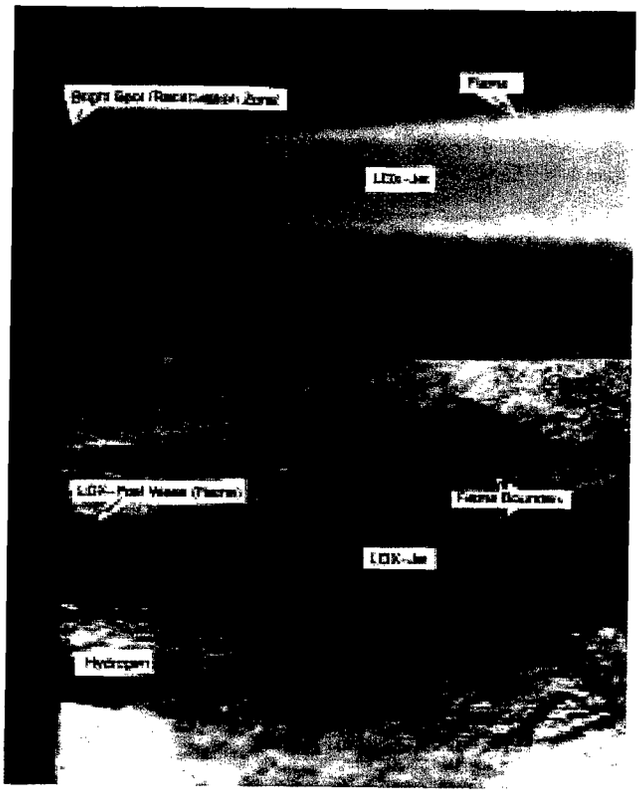

Figure 3: Near injector region of a reacting liquid-oxygen–gaseous-hydrogen shear-coaxial injector, flame (top) and corresponding flow field (bottom). Oxygen and hydrogen velocities are 30 and 300 m/s, respectively, oxygen and hydrogen injection temperatures are 100 *K* and 300 *K*, oxygen jet diameter is 1 *mm*, chamber pressure is 4.5 *MPa* (44 atm). From Mayer and Tamura (1996). Used with permission.

respectively. Note that the critical pressure and temperature of oxygen are p_c = 5.04 *MPa* (49.7 atm) and T_c = 155 *K*, respectively. The critical pressure and temperature of hydrogen are p_c = 1.30 *MPa* (12.8 atm), T_c = 33.2 *K*. When liquid-oxygen is injected at low-subcritical pressures (Fig. 1) atomization occurs forming a distinct spray as described above. Ligaments are detached from the jet surface forming spherical drops which subsequently breakup and vaporize. As the chamber pressure approaches the thermodynamic critical pressure of the liquid-oxygen (Fig. 2), the number of drops present diminishes. Here, the injected jet exhibits a pure diffusion mechanism at a pressure of 4.5 *MPa*, which is slightly below the thermodynamic critical pressure of oxygen, and significantly above that of hydrogen. Experimental results have revealed that flame attachment occurs instantaneously after ignition in the small but intensive recirculation zone which forms just downstream of the annular post. A well mixed diffusion flame forms within this region producing a wake that separates the oxygen stream from the hydrogen-rich outer flow. The conditions imposed for Test Cases RCM-2 and RCM-3 are phenomenologically analogous to those of Figs. 1 and 2.

Flow Characteristics

Simulating either of the two extremes described above with either LES or RANS based methods requires a detailed representation of the broadband turbulence coupled with appropriate multiphase, thermochemical, thermodynamic and transport models. Modeling subcritical atomization and dense spray processes similar to those depicted in Fig. 1 are still one of the most difficult and evasive topics of research. At this point only relatively crude highly empirical models exist. Dilute spray models, however, are more prevalent and can be very accurate at low subcritical pressures. Results shown in subsequent sections will demonstrate the effectiveness of LES in treating dilute spray dynamics in a configuration which eliminates the ambiguities associated with atomization. Simulating the transcritical jet, on the other hand, does not require use of an atomization model, but does require a detailed representation of the physical properties.

Because the fluid is much denser, the broadband turbulence characteristics which must be considered are clearly evident in Fig. 2. Figure 3 is a visualization which illustrates the near injector region of this case in the vicinity of the liquid-oxygen post. The mean flame characteristics are shown on the top of the figure, and the corresponding flow field is shown on the bottom. The oxygen and hydrogen velocities for this case are 30 and 300 m/s, respectively, the oxygen and hydrogen injection temperatures are 100 K and 300 K, the oxygen jet diameter is 1 *mm*, and the mean chamber pressure is 4.5 *MPa* (44 atm). Figures 4 and 5 show the corresponding thermophysical behavior of of oxygen and hydrogen over the regimes of interest. Plots of density, specific heat, viscosity, and thermal conductivity are given on the interval $40 \leq T \leq 1000\ K$ for pressures of 1, 10, 50, 100, 200, and 400 atmospheres. Note that at 1000 K and above, both oxygen and hydrogen exhibit ideal gas behavior and the pressure effect is negligible. As the temperature is decreased below 1000 K, however, significant nonidealities are introduced, with property variations associated with oxygen producing the most significant effects.

Figure 6 shows the trends associated with the kinematic viscosity. The effect of pressure on this quantity is particularly significant and has a direct impact on the characteristic scales associated with the turbulence field. For both oxygen and hydrogen, an increase in pressure from 1 to 100 atmospheres results in a corresponding reduction in the kinematic viscosity of up to three orders of magnitude. This implies a three order of magnitude increase in the characteristic Reynolds number. Based on Kolmogorov's universal equilibrium theory (Tennekes and Lumley 1972, Hinze 1975), the order of magnitude of the Kolmogorov microscale, denoted here as η_t, and the Taylor microscale, denoted here as λ_t, are related to the Reynolds number by

$$\frac{\eta_t}{l_t} \sim Re_t^{-\frac{3}{4}} \qquad \frac{\lambda_t}{l_t} \sim Re_t^{-\frac{1}{2}} \tag{1}$$

Here the Reynolds number is defined as $Re_t = q_t l_t/\nu$ where $q_t = \sqrt{2k_t/3}$. The term q_t represents the turbulence intensity, k_t the *sgs* kinetic energy, and l_t the integral length scale. The relations given by Eq. (1) indicate that a three order of magnitude decrease in the kinematic viscosity results in 2.25 and 1.5 order of magnitude decreases in the Kolmogorov and Taylor microscales, respectively. These reductions have a direct impact on the overall grid density required to resolve key processes.

Figure 7 shows the trends associated with the effective mass diffusivity. When the pressure is increased from 1 to 100 atmospheres, both oxygen and hydrogen exhibit a two order of magnitude decrease in the mass diffusion rate over the full range of temperatures plotted. Oxygen exhibits a decrease of up to 4 orders of magnitude at temperatures below the critical mixing temperature. The diminished mass diffusion rates coupled with the liquid-like densities which dominate at high pressures significantly alter the coupling associated with local combustion characteristics in the vicinity of the liquid-oxygen jet.

Qualitative analysis of Fig. 3 correlated with the trends shown in Figs. 4–7 suggests that there are at least seven fundamentally important flow characteristics which must be accounted for: 1) dense near-critical and supercritical fluid mixture properties, 2) transient broadband turbulent mixing over a wide range of scales, 3) high pressure chemical kinetics, 4) strong multicomponent property gradients, 5) dominant preferential diffusion processes, 6) anomalous multiphase interfaces, and 7) geometrically dominated (wall-bounded) three-dimensional evolution. Treating this set of characteristics represents a minimal requirement for any simulation-based or modeled treatment of the flow. In general, the intricate multiple-time, multiple-length scale coupling must be resolved (or modeled) to represent the physics. A time-accurate treatment of turbulence, thermochemistry, thermodynamics and transport properties are essential, and disparate turbulence and molecular transport processes must be treated simultaneously. Algorithm design and high-performance massively parallel computing are also essential elements.

Modeling Options and Tradeoffs

There are currently three basic choices with regard to the simulation approach. The widely used Reynolds-Averaged Navier-Stokes (RANS) approximation, Large Eddy Simulation (LES) and Direct Numerical Simulation (DNS). The least numerically intensive is RANS. For this approach, all turbulent motions are modeled. The closure is empirical and based on scaling arguments which apply only in the time-averaged limit. In general, predictions are highly sensitive to models and model constants, and respective constants must be adjusted and tuned for every flow. LES is a much more numerically intensive methodology, but offers a higher degree of accuracy in return. For this approach,

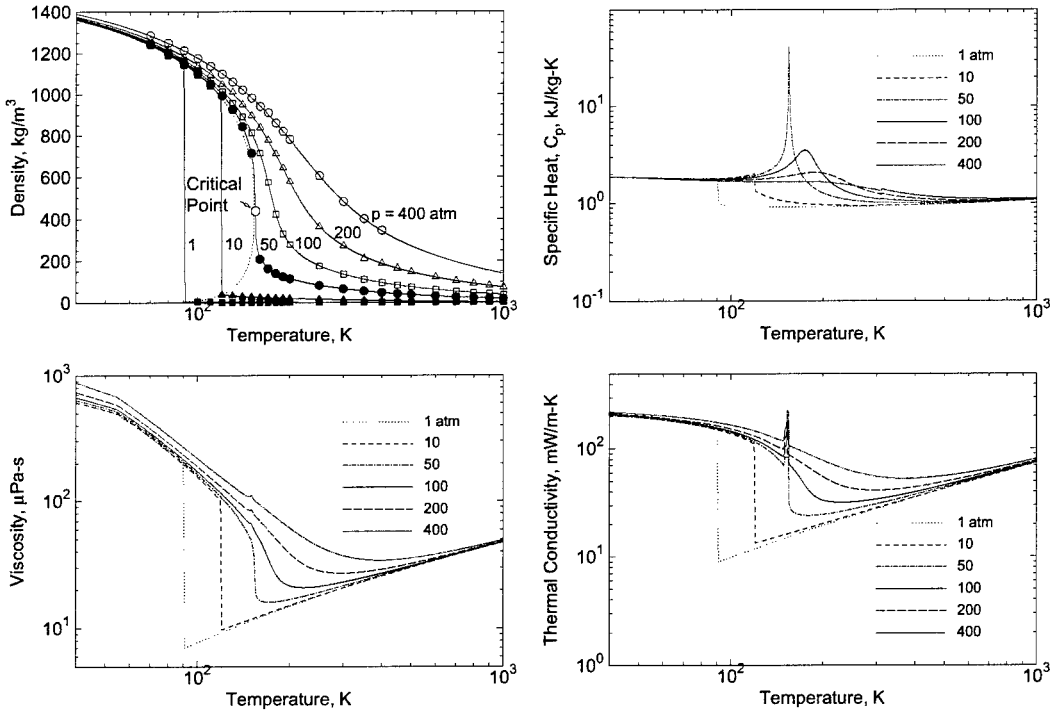

Figure 4: Density (compared with experimental data points obtained by Vargaftik (1975)), specific heat, viscosity, and thermal conductivity versus temperature over the interval $40 \leq T \leq 1000$ and pressures of 1, 10, 50, 100, 200, and 400 atmospheres for pure oxygen.

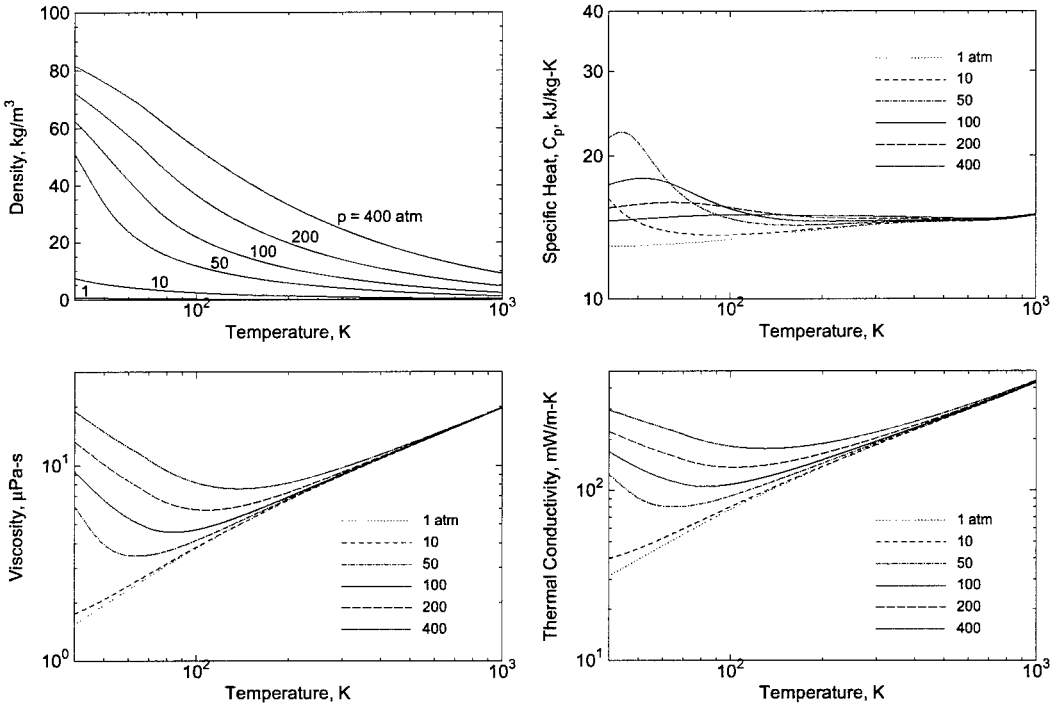

Figure 5: Density, specific heat, viscosity, and thermal conductivity versus temperature over the interval $40 \leq T \leq 1000$ and pressures of 1, 10, 50, 100, 200, and 400 atmospheres for pure hydrogen.

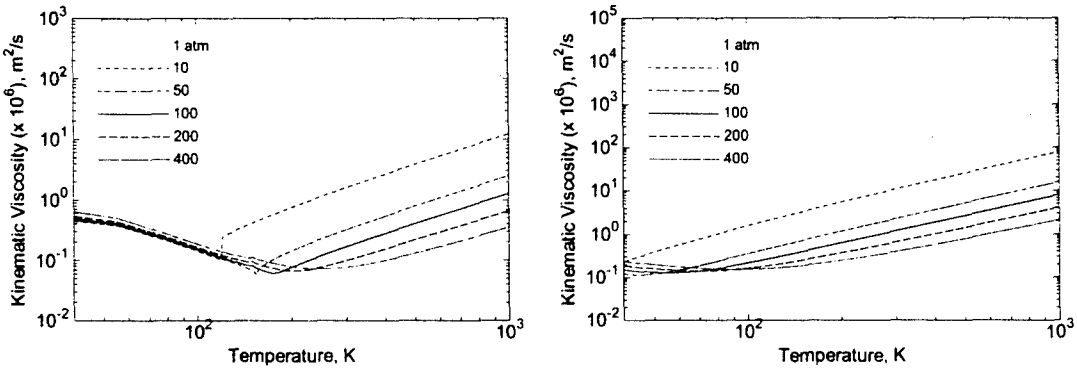

Figure 6: Kinematic viscosity of pure oxygen (left) and pure hydrogen (right) over the temperature interval $40 \leq T \leq 1000$ and pressures of 1, 10, 50, 100, 200, and 400 atmospheres.

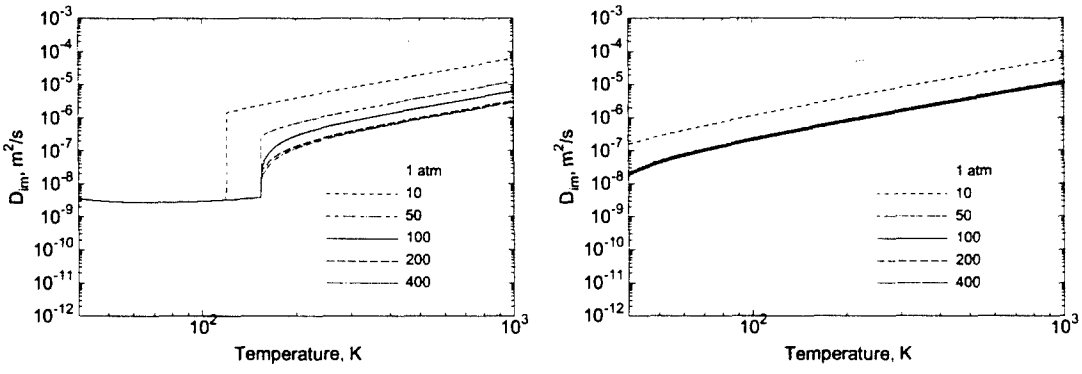

Figure 7: Effective mass diffusivity of pure oxygen (left) and pure hydrogen (right) over the temperature interval $40 \leq T \leq 1000$ and pressures of 1, 10, 50, 100, 200, and 400 atmospheres.

the large energetic scales are resolved, and the subgrid-scales are modeled. In contrast to RANS, LES closures are time-accurate, the models tend to be more universal, and it is not necessary to adjust constants for every flow. With the appropriate grid constraints in place, the use of dynamic modeling eliminates the need for any model constants. The enhanced accuracy, however, comes with a much stricter set of algorithmic requirements. Similarly, DNS is the most numerically intensive. For this approach, all scales are resolved, and no modeling is required, but the method is severely CPU limited.

There are three baseline considerations which currently dictate the selection of RANS versus LES versus DNS as a solution method: 1) the time required to get a solution, 2) the accuracy of a solution, and 3) the feasibility of obtaining a solution. Performing a DNS which meets the seven criteria listed in the previous section is clearly not feasible at this point in time. Thus, tradeoffs typically revolve around RANS versus LES, with DNS being used as a more fundamental tool for studying extremely small-scale phenomena in highly idealized domains. This in itself is limiting, and care must be taken to insure DNS simulations of this type are truly relevant to the flow phenomena of interest. LES, by definition, is an inherently three-dimensional simulation methodology (as is DNS), and LES grid requirements are much stricter than those for RANS. Well proportioned LES grids are typically sized a factor of four coarser in each coordinate direction than an equivalent well sized DNS grid with the equivalent order of accuracy. Examples of well sized LES grids are given in subsequent sections. RANS is by far the fastest solution technique, but also the least accurate since the entire system is essentially a model. However, the speed and minimal resources with which RANS solutions can be obtained is often an invaluable and necessary engineering tool. A secondary consideration is the fact that the LES methodology imposes a much stricter set of numerical requirements and constraints.

General Requirements for LES

Improvements in computational speed and capacity over the past several years has made the application of LES feasible for increasingly complex flows. This method has now been used successfully as both as a complementary tool for understanding turbulence and for modeling the effects of turbulence in a variety of engineering applications. With the advent of massively parallel computer hardware, LES now provides a means to study coupled combustion, transport and multiphase processes in parameter spaces that are unattainable using direct numerical simulation (DNS) techniques, with a degree of fidelity that can be far more accurate than other conventional methods.

Modeling Issues

During the past decade, considerable progress has been made in LES. Early works relied heavily on the use of the Smagorinsky eddy viscosity model (Smagorinsky 1963). A key breakthrough in the field of *sgs* modeling resulted from the introduction of the dynamic modeling procedure (Germano, Piomelli, Moin and Cabot 1991, Moin, Squires, Cabot and Lee 1991, Lilly 1992, Zang, Street and Koseff 1993, Vreman, Geurts and Kuerten 1994). In this approach constants which appear in the base *sgs* models are computed dynamically as functions of space and time providing the proper local amount of *sgs* scalar mixing and dissipation. Another important idea in *sgs* modeling involves the use of scale-similarity laws which assume that the largest of the unresolved scales have similar structure to the smallest of the resolved scales. Among these models, only that proposed by Bardina, Ferziger and Reynolds (1983) satisfies the important physical constraint of Galilean invariance (Speziale 1985).

Dynamic modeling coupled with scale similarity ideas have been very useful in *sgs* modeling of nonreacting flows. This concept is currently being exploited in LES of reacting flows. Erlebacher, Hussaini, Speziale and Zang (1992) were one of the first to propose a compressible generalization of the dynamic Smagorinsky model and couple this to the scale-similarity model to obtain the *sgs* mass and energy fluxes. These ideas have now been extended to multicomponent mixtures (Oefelein 2001). With this framework in place, the role of combustion models are to account for the effect of *sgs* fluctuations in the thermochemical variables and filtered chemical source terms over a wide range of pressures. Achieving this closure hinges on the specification of accurately reduced kinetics mechanisms coupled to an accurate representation of *sgs* scalar mixing processes.

Numerical Constraints

It is well known that numerical dissipation and dispersion errors can have significantly devastating effects on *sgs* models. The presence of these errors depletes energetic turbulence scales at the mid- to high-wavenumbers and consequently competes with the models. When this occurs, the *sgs* models themselves often have no effect on the flow, and the contamination often to leads erroneous conclusions. To avoid this situation, numerical methods used for LES must provide spatially "non-dissipative" spectrally clean damping characteristics out to the smallest wavenumbers coupled with simultaneous local conservation of mass, momentum and total-energy. Conservation of kinetic energy is particularly important when dynamic modeling is used.

Co-located schemes with explicit artificial dissipation terms added for stabilization purposes have historically failed to provide the appropriate spectral characteristics. This is easily shown if one compares the magnitude of the residual associated with the artificial dissipation terms of a given scheme to that associated with a given *sgs* model. The former is always orders of magnitude greater, even for higher-order schemes. Unfortunately, this fact precludes a wide class of flow solvers, including the trivial conversion of most RANS based codes. Staggered grid algorithms fashioned after the pioneering work of Harlow and Welch (1965), on the other hand, have been shown to give acceptable spectral characteristics. Specialized schemes of this type are currently the workhorse of the LES community.

Because of the obvious advantages, grid stretching functions are widely used for LES just as they are for RANS calculations. One additional constraint associated with LES, however, is that the energetic scales must be resolved on grids that minimize commutation errors. This requirement imposes strict grid stretching constraints which precludes the use of typical RANS grids. Instead, grids must be constructed with much more restricted grid stretching and grid aspect ratios. The stretching ratio associated with adjacent cells in a given coordinate direction should never exceed 10 percent, and grid aspect ratios greater than 100 are rarely acceptable. The issues outlined above represent minimal requirements and non-adherence can lead to diminished broadband resolution and significant high wavenumber contamination.

Phenomenological Case Studies

Development efforts conducted by Oefelein (2001) over the past several years have led to a massively parallel software package which incorporates the general requirements for LES described in the previous section. The effort was driven by two mutually dependent objectives. The first was to develop improved models suitable for performing high-fidelity LES of the complex phenomena described above. The second was to develop a high-performance parallel algorithm which supported the implementation of large-scale simulations. Emphasis was placed on a general treatment of phenomenologically complex reacting multiphase flows, including the seven fundamentally important flow characteristics described above. These flow characteristics are:

1. Dense near-critical and supercritical fluid mixture properties.
2. Broadband turbulent mixing over a wide range of scales.
3. High pressure chemical kinetics.
4. Strong multicomponent property gradients.
5. Dominant preferential diffusion processes.
6. Anomalous multiphase interfaces.
7. Geometrically dominated (wall-bounded) three-dimensional evolution.

The baseline Eulerian–Lagrangian framework solves the filtered conservation equations of mass, momentum, total-energy and species using a staggered grid methodology analogous to that pioneered by Harlow and Welch (1965) in generalized curvilinear coordinates. Dual-time stepping is used with a unified all Mach number preconditioning technique. The algorithm accommodates fully implicit time advancement using a fully explicit multistage scheme in pseudo-time. This scheme exhibits excellent parallel efficiency and scalability attributes. The implicit formulation is

A-stable which allows one to set the time step based solely on accuracy considerations. It accommodates arbitrary equations of state, thermochemical, thermodynamic and transport processes, and provides full thermophysical coupling over a wide range of conditions. It accommodates intermediate complex geometric features while maintaining the accuracy of structured spatial stencils. The parallel paradigm employs distributed-memory message-passing using MPI, the single-Program–Multiple-Data (SPMD) model and structured multiblock domain decomposition.

Following are three examples which give insight into the intricate nature of the problem and the current state of the art with respect to LES. The first is an early set of results which illustrate the prevalence of items 1-7 listed above when modeling high pressure mixing and combustion in liquid-oxygen (LOX), hydrogen systems. These results represent a first preliminary attempt at simulating these phenomena and demonstrate a capability to handle the extreme complex thermophysical flow characteristics. The second example is an LES of a low-Mach-number, high-Reynolds-number, particle-laden channel flow. This is an extremely difficult case to handle with a compressible flow solver. The results demonstrate a capability to handle these extremes, the ability of LES to capture transient broadband turbulent mixing over a wide range of scales, and also the ability to resolve the geometrically dominated (wall-bounded) three-dimensional evolution of the flow. The last set of results also demonstrates these advantages in a more complex geometry, and additionally the ability of LES to simulate spray characteristics and particle dispersion.

High-Pressure Mixing and Combustion in LOX–H_2 Systems

Figure 8 shows contours of density, temperature, and H_2, O_2, OH and H_2O mass fractions in the near-field injector region of a hydrogen–liquid-oxygen shear layer. The two streams are separated by a 0.5 *mm* LOX post. The pressure is 10.1 *MPa* (100 atm). The hydrogen (upper stream) and oxygen (lower stream) velocities are 125 and 30 m/s, respectively. The injection temperatures are 150 *K* and 100 *K*. These early calculations were performed using the theoretical-numerical framework developed by Oefelein (1997) and represent a first attempt at simulating such processes. The matrix of conditions considered were fashioned after the flow visualization studies conducted by Mayer and Tamura (1996). Emphasis was placed on the near-field flow processes in the vicinity of the post. The conditions selected produce a supercritical hydrogen stream and a liquid-oxygen stream which undergoes a transcritical change of state within the mixing layer. Inlet velocity profiles were generated assuming fully developed turbulent flow and a heat conduction model was applied to the splitter plate to provide a realistic energy flux distribution at the walls. Nonreflecting outflow conditions were imposed at the exit and inviscid, adiabatic, and noncatalytic conditions were imposed at the transverse boundaries.

These results illustrate the prevalence of items 1-7 listed above. Transcritical mixing induces a vortical structure within the injected hydrogen stream which is analogous to that produced by a backward facing step. This structure emanates from the boundary layer upstream of the post and is amplified by interactions within the shear layer and coalescence downstream with adjacent vortices. The oxygen stream, on the other hand, proceeds unimpeded in an essentially straight line. Because of the liquid-like characteristics of the oxygen stream, an extremely large density gradient exists within this region. Note that the change in density is on the order of 1000 to 1. Diminished mass diffusion rates are also evident. The combined effect produces a fuel rich flame which anchors itself to the oxygen jet and behaves in a qualitatively similar manner as the diffusion dominated flame depicted in Figs. 2 and 3. Combustion occurs at near stoichiometric conditions and produces a wake which effectively separates the hydrogen and oxygen streams as the flow evolves downstream. Results highlight the effect of the momentum flux ratio on flame-holding dynamics, the dominating effect of the density gradient, and the impact of diminished mass diffusion rates which accompany the liquid-like behavior of near-critical fluids.

Low-Mach-Number, High-Reynolds-Number (Particle-Laden) Channel Flow

Three particularly relevant effects induced by interphase coupling are turbulence modulation which involves the damping of gas phase turbulence by particulates accommodating to turbulent motion, turbulence generation which involves the production of gas phase turbulence due to the presence of particle wakes, and liquid deformation and breakup processes and the resultant effect on interphase exchange processes. As part of an effort to treat these phenomena systematically a series of LES calculations are being performed using the algorithmic framework describe above and compared to the experimental data acquired by Kulick, Fessler and Eaton (1994). These experiments characterize the interactions between various particle loading conditions and the fluid turbulence in the well-defined confines of a turbulent channel. Particles are selected to respond to some, but not all scales of turbulent motions. Gas phase velocities were measured to investigate the means by which particles attenuate turbulence.

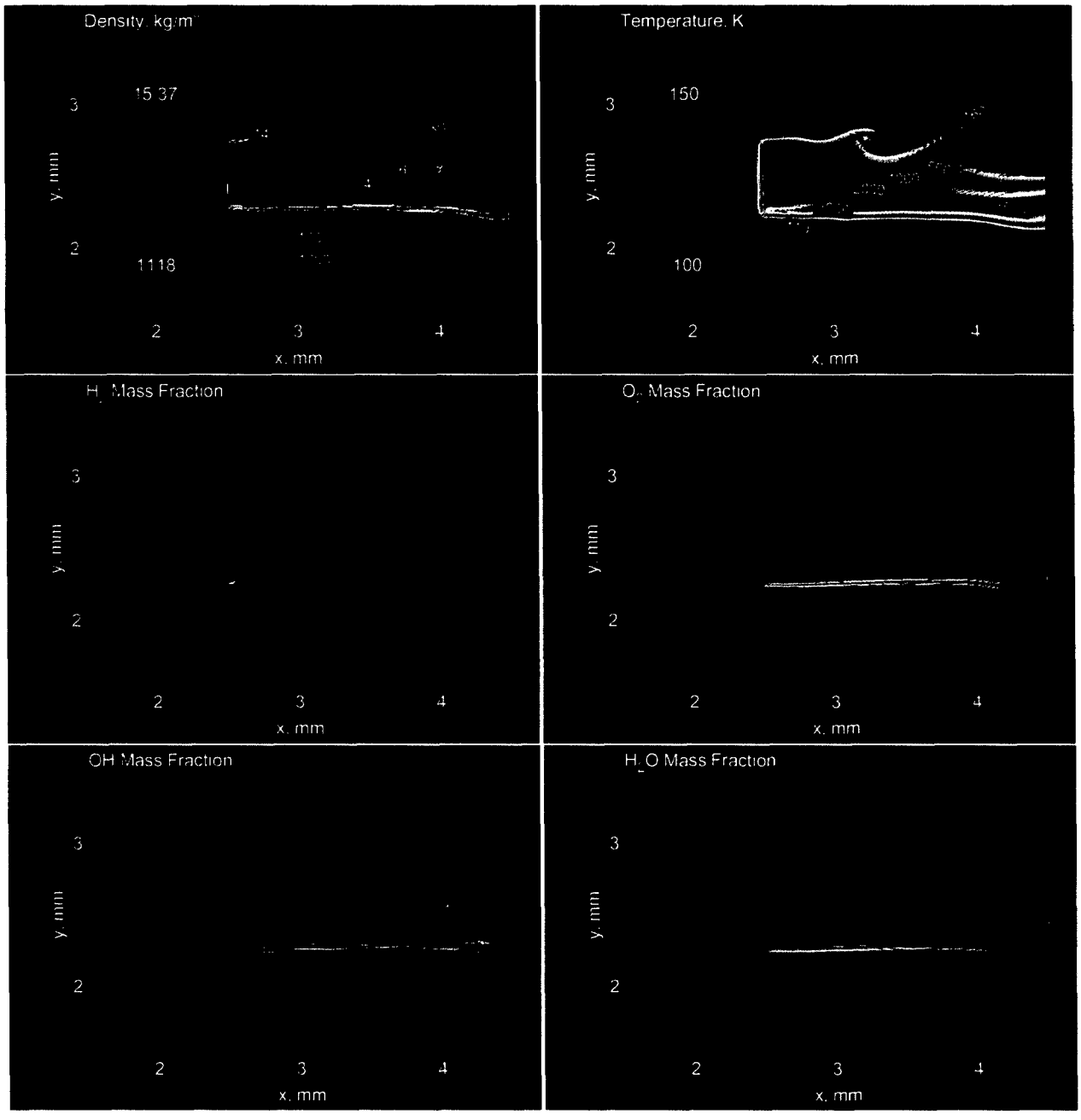

Figure 8: Contours of density, temperature, and H_2, O_2, OH and H_2O mass fractions in the near-field injector region. Chamber pressure is 10.1 *MPa* (100 atm), hydrogen (upper stream) and oxygen (lower stream) velocities are 125 and 30 m/s, respectively, and injection temperatures are 150 *K* and 100 *K*.

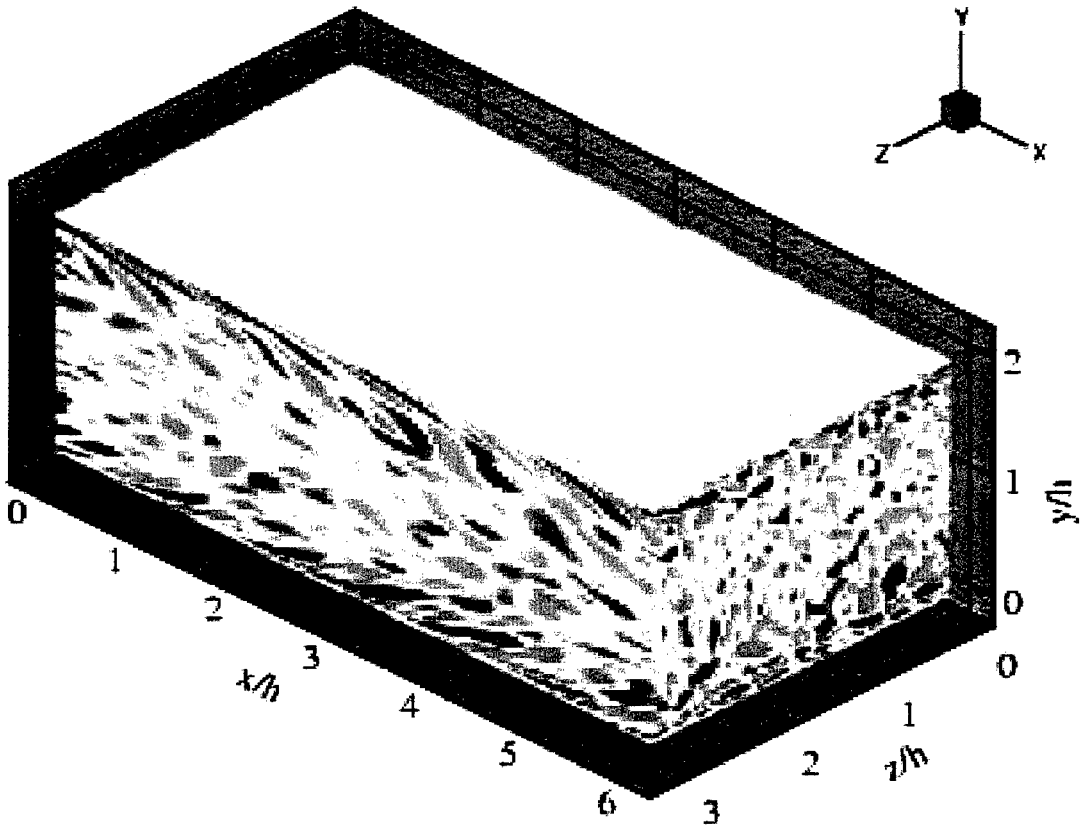

Figure 9: Instantaneous contours of the streamwise component of vorticity in a high Reynolds number, particle laden channel. Half-height is $h = 20\ mm$, mean centerline velocity is $U_{\mathrm{cl}} = 10.5\ m/s$, Reynolds number based on h is $\mathrm{Re}_h = 13800$, friction velocity is $u_\tau = 0.49\ m/s$ and Reynolds number based on u_τ is $\mathrm{Re}_\tau = 645$.

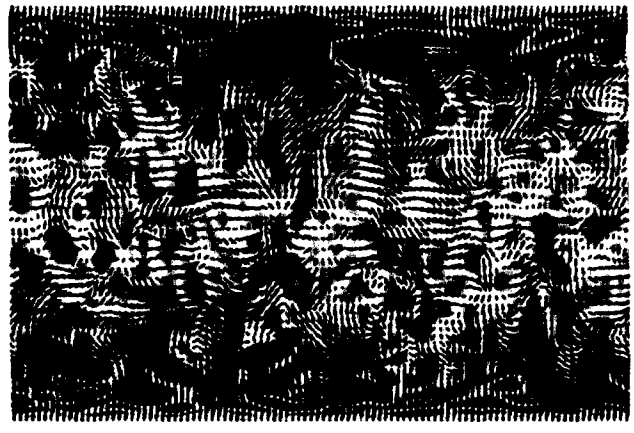

Figure 10: Velocity vectors and contours of the streamwise component of vorticity in the $y - z$ plane.

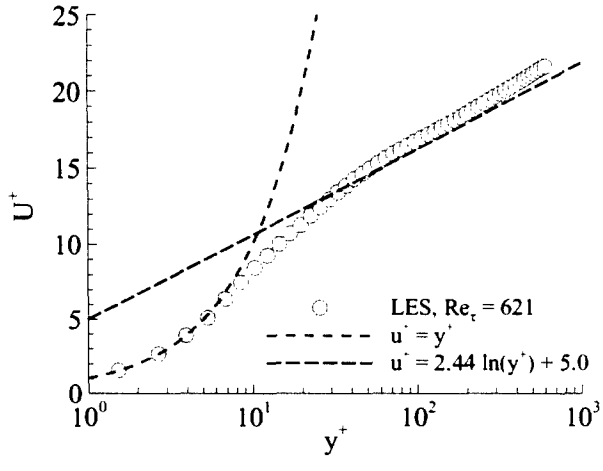

Figure 11: Time-averaged streamwise component of velocity compared with classic law-of-the-wall profiles.

Figure 9 shows the instantaneous contours of the streamwise component of vorticity in the turbulent low-Mach-number, high-Reynolds-number, particle laden channel of Kulick et al. (1994). The channel half-height is $h = 20\,mm$. The mean centerline velocity is $U_{\rm cl} = 10.5\,m/s$ and the Reynolds number based on h is $\mathrm{Re}_h = 13800$. The friction velocity is $u_\tau = 0.49\,m/s$ and Reynolds number based on u_τ is $\mathrm{Re}_\tau = 645$. The domain dimensions in the streamwise, transverse (wall-normal), and spanwise directions, respectively are $6h \times 2h \times 3h$. The primary grid is composed of 100^3 hexahedral cells.

This second set of results demonstrate the ability of LES to capture transient broadband turbulent mixing over a wide range of scales and the ability to resolve the geometrically dominated three-dimensional evolution of turbulent flows. It also demonstrates the ability of the algorithmic framework to handle low-Mach-number flows in the incompressible limit. The detailed broadband structure associated with the baseline conditions described above are shown in Fig. 10. Here velocity vectors are plotted with contours of the streamwise component of vorticity in the $y - z$ plane. Figures 11 and 12 show the time-averaged streamwise component of velocity compared with classic law-of-the-wall profiles and the streamwise and wall-normal root-mean-square components of velocity compared with experimental data points obtained by Kulick et al. (1994). These results are typical when dynamic modeling is used with an appropriately sized grid.

Swirling Particle-Laden Flow in Coannular Dump-Combustor

In addition to broadband turbulence structure, this last set of results demonstrates the ability of LES to simulate spray characteristics and particle dispersion. Obtaining high-fidelity solutions of reacting sprays hinges on the application

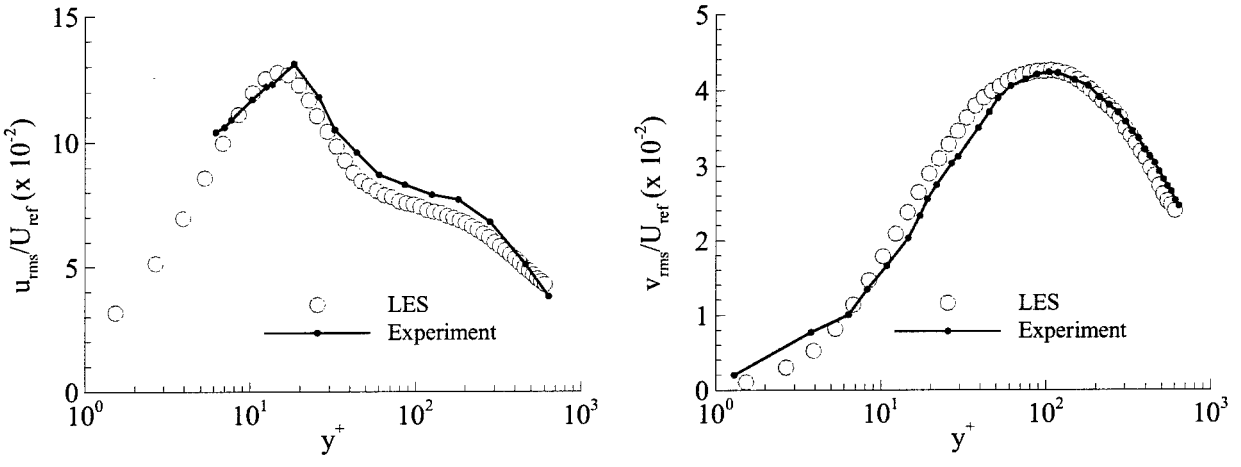

Figure 12: Streamwise and wall-normal root-mean-square components of velocity compared with experimental data points obtained by Kulick et al. (1994).

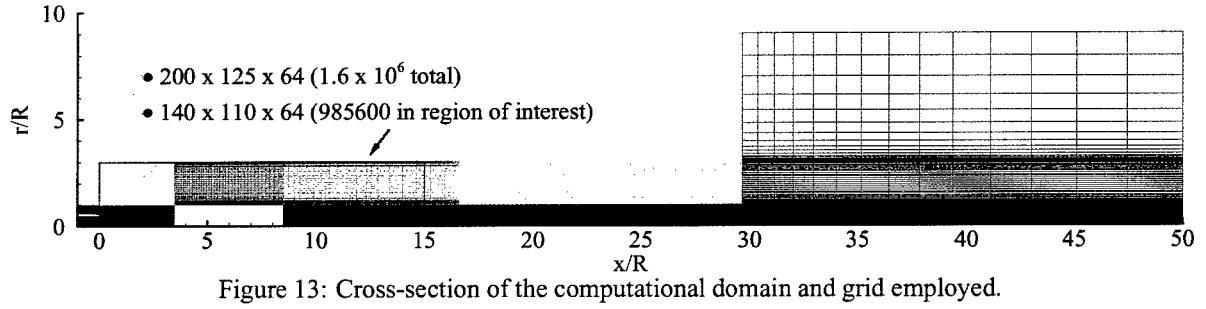

Figure 13: Cross-section of the computational domain and grid employed.

of methods and models which accurately describe momentum coupling and subgrid-scale modulation of turbulence, mass and energy coupling and subgrid-scale scalar mixing, and the combustion processes induced as a consequence. As part of an effort to treat these phenomena systematically a series of LES calculations have been performed and compared to the experimental data acquired by Sommerfeld et al. (Sommerfeld and Qiu 1991, Sommerfeld, Ando and Wennerberg 1992, Sommerfeld and Qiu 1993). These experiments characterize a swirling particle-laden flow in a model coannular combustion chamber and effectively isolate the effects related to momentum coupling. The primary objectives here were to gain a clearer understanding of the effectiveness and feasibility of current models and to gain a quantitative understanding of potential model limitations by analyzing the characteristic fluid dynamic scales of importance.

Sommerfeld et al. provides detailed measurements of swirling particle-laden flow in a chamber which consists of a sudden pipe expansion with a centered (primary) and annular (secondary) jet discharging into a cylindrical test section. A cross-section of the computational domain is given in Fig. 13. The region of interest is shown in Fig. 14. The primary jet has a radius of $r/R = 0.5$ and is laden with glass beads with a mean particle diameter of 45 μm distributed between 20 and 80 μm. The secondary jet extends over a radial interval of $0.59 \leq r/R \leq 1$ and is injected with a swirling azimuthal velocity component. The relevant flow conditions and particle properties are summarized in Table 1. Particles are injected in the primary jet in equilibrium with the gas-phase in a manner that matches the experimental distribution. A series of one-component phase-Doppler anemometer measurements were made along cross-sections at the 8 axial locations indicated. Gas-phase and particle-phase mean and rms velocity components were acquired along with simultaneous measurements of the particle size and mass flux distributions.

Figure 15 shows 1 mm thick cross-sections of the instantaneous particle distributions for Case 2 superimposed on the corresponding turbulent velocity field. For plotting purposes, the superimposed particle distribution shown is quite thick relative to the particle size distribution. One should not infer from this figure that collisions are important. Analysis of the particle number densities throughout the flowfield indicate that they are not. At any instant in time there are approximately 2.5 million particles being tracked, with two-way coupling applied between the gas and particles.

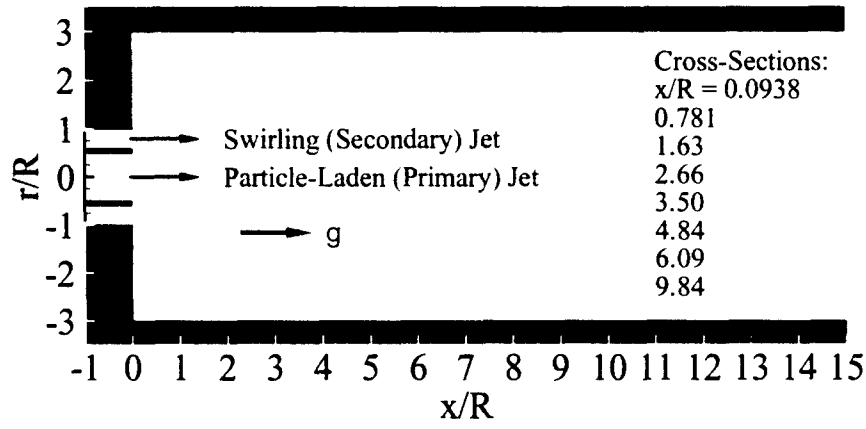

Figure 14: Region of interest in the Sommerfeld configuration.

Table 1: Flow conditions and particle properties used in the Sommerfeld experiments.

	Case 1	*Case 2*
Gas Phase (Air):		
Flow rate in primary jet, g/s	9.9	6.0
Flow rate in secondary jet, g/s	38.3	44.6
Inlet Reynolds number[a]	26200	27250
Swirl number	0.47	0.49
Temperature, K	300	
Particle Phase:		
Loading ratio in primary jet	0.034	0.17[b]
Flow rate, g/s	0.34	1.0
Mean diameter, μm	45.5	
Density ratio, ρ_p/ρ_f	2152	

[a] Based on total volume flow rate.

[b] 5 × Case 1.

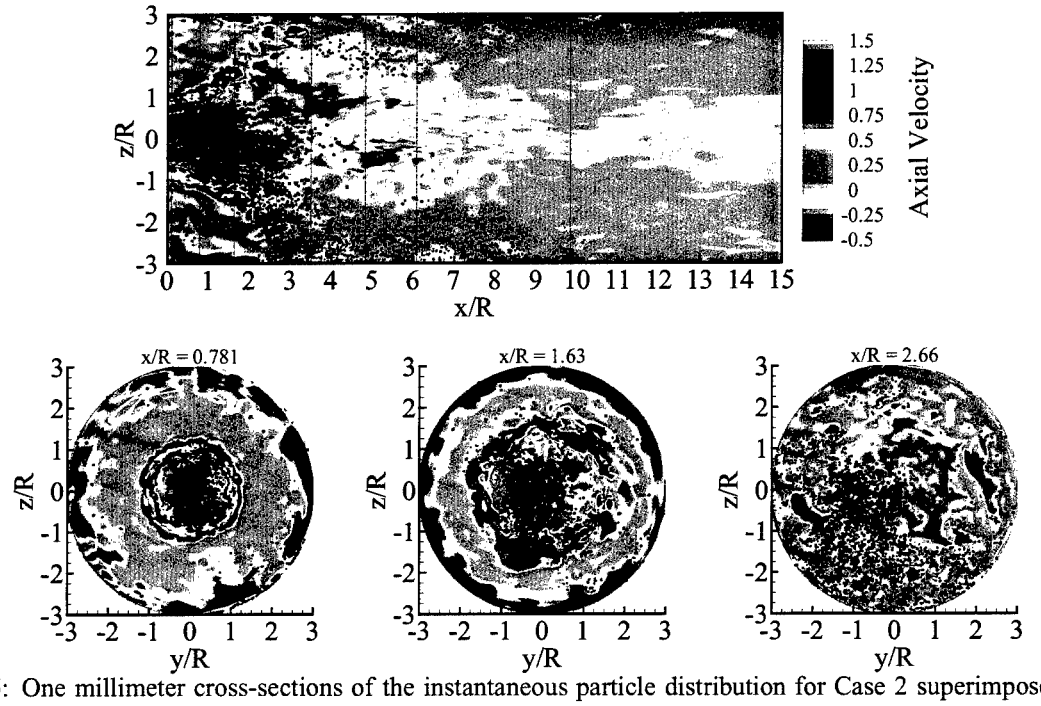

Figure 15: One millimeter cross-sections of the instantaneous particle distribution for Case 2 superimposed on the corresponding turbulent velocity field ($R_{ref} = 32\,mm$, $U_{ref} = 12.9\,m/s$).

Tracking this number of particles is significant since it verifies the feasibility of employing large numbers of physical particles and eliminates the need to implement classical "parcel" approximations.

The mean flow characteristics for Cases 1 and 2 are shown in Fig. 16. This figure shows the time-averaged, azimuthally-averaged gas-phase velocity field. Key features of the flow include primary and secondary recirculation zones, a stagnation point in the core region and a reattachment point on the outer wall. The location of these points coincide with measured results to within 5 % for both cases. Figure 17 shows representative comparisons of (a) the mean axial gas velocity, (b) the corresponding mean axial particle velocity, (c) the mean particle diameter, and (d) the mean particle momentum flux for Case 2 at respective axial stations. The agreement between the measured and calculated results is excellent and similar agreements have been obtained with respect to the entire experimental data set.

After validating the LES methodology with the Sommerfeld data subsequent calculations were performed within the same configuration to gain a more quantitative understanding of the relevant modeling issues. Here, the validated broadband characteristics inherent to the LES methodology were used to obtain additional data that could not be

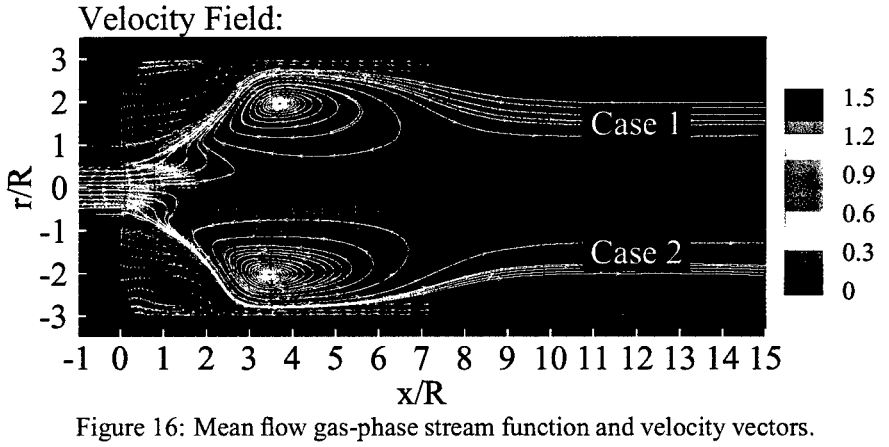

Figure 16: Mean flow gas-phase stream function and velocity vectors.

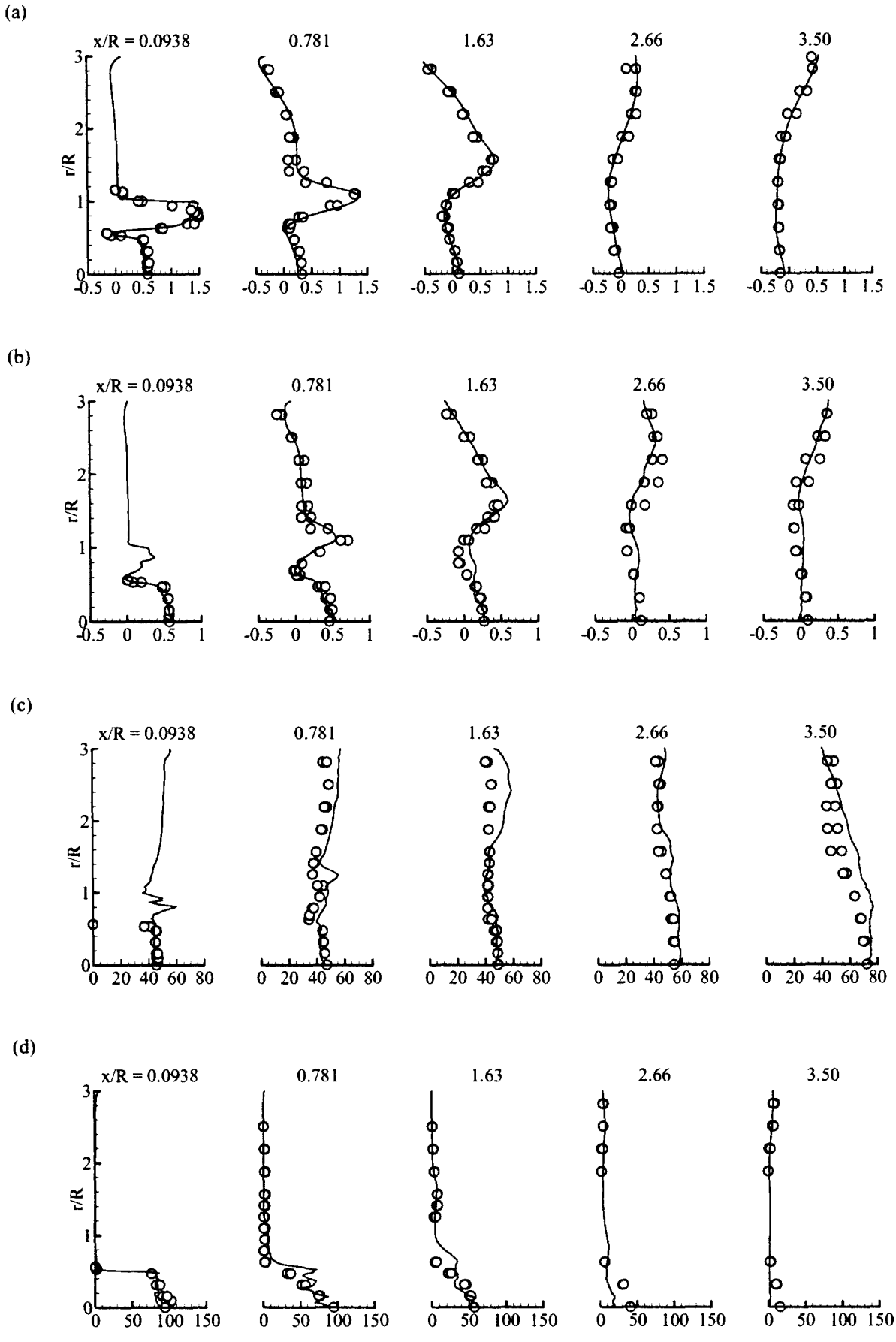

Figure 17: Comparisons of measured (o) and calculated (—) time-averaged profiles of (a) the mean axial gas velocity, (b) the corresponding mean axial particle velocity, (c) the mean particle diameter, and (d) the mean particle momentum flux for Case 2.

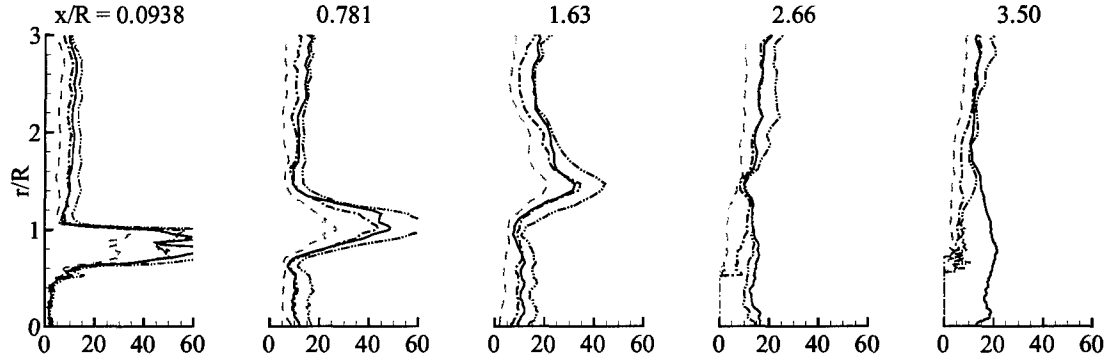

Figure 18: Mean particle Reynolds number corresponding to Case 2: (−) all classes; (--) $d_p = 30 \pm 5\ \mu m$; (−) $d_p = 45 \pm 5\ \mu m$; (−) $d_p = 60 \pm 5\ \mu m$.

acquired from the experiment. In addition to the enhanced quantitative insight, this data was used to determine the envelope of conditions to be characterized by the model development effort. Figure 18 presents a representative set of results. Here profiles of the mean particle Reynolds number for Case 2 are given at respective axial stations for all size classes, $d = 30 \pm 5\ \mu m$, $d = 45 \pm 5\ \mu m$, and $d = 60 \pm 5\ \mu m$. Other key scales and parameters obtained include 1) particle characteristics such as the particle number density, volume fraction, Sauter mean diameter etc., 2) flow characteristics such as the turbulence intensity, Kolmogorov microscales and Taylor microscales, and 3) time-scales such as the Stokes number and particle relaxation time.

Conclusions

Improvements in computer speed and capacity have made application of the large eddy simulation technique feasible for increasingly complex flows. The discussion and results presented have outlined the key phenomenological trends and have demonstrated model performance and accuracy requirements. Results have also highlighted various intricacies associated with transcritical and supercritical phenomena, highlighted the effect of pressure on near-critical mixing and combustion processes, and provided increased insights into the theoretical and numerical methodologies employed. Currently, coupled turbulent mixing and the treatment of thermodynamic and transport processes in laboratory-scale geometries can be handled quite accurately. The treatment of dilute spray dispersion and vaporization processes are also handled well. Accurate treatment of turbulent premixed and non-premixed flame phenomena, on the other hand, is still pending, as is the treatment of atomization processes and interface dynamics. The latter still lacks a strong theoretical basis. Current efforts are focused on model assessment and validation at realistic device-scale conditions and analysis of validated systems to systematically characterize the relevant time-scales, length-scales, and other key parameters which are of direct importance to sgs model development.

References

Bardina, J., Ferziger, J. H. and Reynolds, W. C. (1983). "Improved Subgrid Scale Models Based on Large Eddy Simulation of Homogeneous, Incompressible, Turbulent Flows," *Technical Report TF-19, Department of Mechanical Engineering*, Stanford University Stanford, California 94305.

Erlebacher, G., Hussaini, M. Y., Speziale, C. G. and Zang, T. A. (1992). "Toward the Large Eddy Simulation of Compressible Turbulent Flows," *Journal of Fluid Mechanics*, **238**: 155–185.

Germano, M., Piomelli, U., Moin, P. and Cabot, W. H. (1991). "A Dynamic Subgrid-Scale Eddy Viscosity Model," *Physics of Fluids*, **3**(7): 1760–1765.

Harlow, F. H. and Welch, J. E. (1965). "Numerical Calculation of Time-Dependent Viscous Incompressible Flow of Fluid with Free Surface," *Physics of Fluids*, **8**(12): 2182–2198.

Hinze, J. O. (1975). *Turbulence* second edn McGraw-Hill New York, New York.

Kulick, J. D., Fessler, J. R. and Eaton, J. K. (1994). "Particle Response and Turbulence Modification in Fully Developed Channel Flow," *Journal of Fluid Mechanics*, **277**: 109–134.

Lilly, D. K. (1992). "A Proposed Modification of the Germano Subgrid-Scale Closure Method," *Physics of Fluids*, **3**(11): 633–635.

Mayer, W. and Tamura, H. (1996). "Propellant Injection in a Liquid Oxygen/Gaseous Hydrogen Rocket Engine," *Journal of Propulsion and Power*, **12**(6): 1137–1147.

Moin, P., Squires, K., Cabot, W. and Lee, S. (1991). "A Dynamic Subgrid-Scale Model for Compressible Turbulence and Scalar Transport," *Physics of Fluids*, **3**(11): 2746–2757.

Oefelein, J. C. (1997). *Simulation and Analysis of Turbulent Multiphase Combustion Processes at High Pressures* PhD thesis The Pennsylvania State University University Park, Pennsylvania 16802.

Oefelein, J. C. (2001). "General Numerical Framework for Reacting Multiphase Flow with Complex Thermochemistry, Thermodynamics and Transport," Copyright 1992-2001 by J. C. Oefelein, All Rights Reserved.

Smagorinsky, J. (1963). "General Circulation Experiments with the Primitive Equations. I. The Basic Experiment," *Monthly Weather Review*, **91**: 99–164.

Sommerfeld, M. and Qiu, H. H. (1991). "Detailed Measurements in a Swirling Particulate Two-Phase Flow by a Phase-Doppler Anemometer," *International Journal of Heat and Fluid Flow*, **12**(1): 20–28.

Sommerfeld, M. and Qiu, H. H. (1993). "Characterization of Particle-Laden, Confined Swirling Flows by Phase-Doppler Anemometry and Numerical Calculation," *International Journal of Multiphase Flow*, **19**(6): 1093–1127.

Sommerfeld, M., Ando, A. and Wennerberg, D. (1992). "Swirling, Particle-Laden Flows through a Pipe Expansion," *Journal of Fluids Engineering*, **114**: 648–656.

Speziale, C. G. (1985). "Galilean Invariance of Subgrid-Scale Stress Models in the Large Eddy Simulation of Turbulence," *Journal of Fluid Mechanics*, **156**: 55–62.

Tennekes, H. and Lumley, J. L. (1972). *A First Course in Turbulence* The MIT Press Cambridge, Massachusetts.

Vargaftik, N. B. (1975). *Tables on the Thermophysical Properties of Liquids and Gases* second edn Wiley New York, New York.

Vreman, B., Geurts, B. and Kuerten, H. (1994). "On the Formulation of the Dynamic Mixed Subgrid-Scale Model," *Physics of Fluids*, **6**(12): 4057–4059.

Zang, Y., Street, R. L. and Koseff, J. R. (1993). "A Dynamic Mixed Subgrid-Scale Model and its Application to Turbulent Recirculating Flows," *Physics of Fluids*, **5**(12): 3186–3195.